Microwave Nondestructive Testing of Nonmetallic Pipes: An Overview of the Major Developments

Reza K. Amineh

Non-metallic and composite components [1]–[3] are rapidly becoming a significant part of various industrial sectors including energy, aerospace, naval, sport, automotive, urban infrastructure, etc. Attractive characteristics of composite components include immunity to corrosion, low cost, low weight, and in some applications their flexural resilience to seismic or dynamic loads. These superior characteristics are leading to the replacement of conventional metallic pipes with composite non-metallic pipes (NMPs) made of fiber-reinforced plastic (FRP), glass-reinforced epoxy resin (GRE), high-density polyethylene (HDPE), reinforced rubber expansion joints (REJs), and carbon fiber-reinforced plastics (CFRP).

Despite these advantages, NMPs are prone to bursting and leakage due to various types of defects caused during fabrication or usage. The leakage of contents from the pipelines could be harmful to the environment, especially if the pipes carry gas or chemicals. It can also interrupt production and distribution processes. Thus, evaluation of these pipes helps in their timely maintenance to avoid catastrophic events. However, despite the recent significant usage growth, the development of suitable nondestructive testing (NDT) technologies for NMPs is lagging. Currently, there is a gap in the NDT industry for fast and robust volumetric imaging of cylindrical composite components, in particular, composite pipes used in the oil and gas industry. While NDT methods have been successfully and widely used for the inspection of metallic pipes, traditional methods are not suitable for the quality control and evaluation of NMPs. On the other hand, the physics of the microwave NDT [4] makes it possible to provide volumetric images of these pipes and measure properties such as wall thickness and eccentricity. Thus, microwave NDT is emerging as a unique and promising method to evaluate defects in a variety of NMPs and vessels (e.g., see [5]). Defects that can be detected include cracks, welding problems, misalignments, disbands, foreign material inclusions, voids, adhesive misapplications, air bubbles, changes in thickness, moisture or other liquid contaminations, mechanical damages, and physical changes due to chemical attacks.

In this article, we first review the significance of microwave NDT for the inspection of NMPs. Then, we review some of the major developments in this area and provide sample results. Some of the techniques that will be discussed will be capable of resolving and evaluating defects on multiple pipes and fitting joints or evaluating the extent of the damage along the radial direction for cylindrical composite components. This information provides valuable assessment means to predict the lifetime of in-service components and helps with their timely maintenance.

Significance of Using NMPs

Carbon steel pipes commonly used in the oil and gas industry are susceptible to corrosion, and oil companies spend significant budgets on expensive corrosion inhibitor chemicals and inspections of these pipes to prevent leaks that interrupt production and harm the environment. Corrosion in oil and gas operations is generally caused by water, carbon dioxide, and hydrogen sulfide and can be aggravated by microbiological activity. Deploying nonmetallic materials in economically and technically feasible applications combats corrosion. Many major oil and gas companies including Saudi Aramco [6] are moving towards the use of NMPs due to their immunity to corrosion. Unlike carbon steel pipes, composite pipes and fittings do not corrode. Saudi Aramco reports that this characteristic alone is worth more than US $1.5 billion per year in terms of corrosion-inhibiting chemicals, replacement of corroded pipes, and corrosion inspection costs.

Common Types of NMPs and Their Failure Modes

Two common types of NMPs are made of FRP and associated products and HDPE. Below, we briefly describe the structure and failure modes for each type [7].

FRP is a plastic matrix reinforced by fine fibers of many different materials. Glass is the most common material, and the corresponding FRP is called fiberglass. Aramid fibers, such as Kevlar, are also becoming more common. Carbon fiber is also gaining popularity because of its high strength. The plastic

1094-6969/24/$25.00©2024IEEE

matrix may be epoxy, thermosetting plastic, or thermoplastic. The most common type of FRP is glass-reinforced plastic (GRP). The advantages of FRP and its associates include being strong, lightweight, corrosion-resistant, cost-effective, and non-conducting.

The failure modes of GPR include:

- Similar to concrete, the plastic matrix used in GRP is fine with the compression but it is weak with the tension. Glass fiber adds tensile strength to some extent.
- Some failure modes are similar to metals. One failure mode is due to the overload. Too much load results in the tearing of glass fiber and often results in delamination.
- Chemical attack can weaken glass fibers, leading to the failing of the components under smaller loads.
- Hydrolysis (unique to GRP) occurs when water or other liquid penetrates the plastic matrix. The interaction with the plastic matrix causes chemical reactions and the formation of acidic molecules. These molecules become mobile and occupy more volume than the original molecules, and pressure builds inside the laminate structure. This internal pressure results in blistering and delamination. Blister formation is typically on the surface and close to the source of liquid. Thus, in pipes, it is internal and not visible.
- Erosion is not unique to GRP. It affects the weaker plastic matrix and leaves the glass fiber.
- Manufacturing issues: Resin-poor regions are weak due to a lack of binders. These areas react differently to the load. On the other hand, resin-rich areas are weak due to low glass content. Poor layup practice could also cause failure.
- Assembly problems: Lack of adhesive or incomplete adhesive can cause problems at joints. These are internal defects that are more difficult to detect.

Furthermore, HDPE piping is used extensively in the petrochemical and utility industries for various services including harsh environment cases. Its use is becoming more prevalent due to its low cost versus steel piping and its ability to withstand corrosive environments. One of the problems with this piping is the current inability to non-destructively examine the weldments. Standard methods, such as radiography and ultrasonics have not been capable of reliably detecting flaws in the weldments [8].

Microwave NDT for the Inspection of NMPs

NMPs offer resistance to corrosion but present challenges to conventional NDT techniques. Developing reliable NDT methods and defect acceptance criteria for quality assurance of NMPs are important steps that are necessary for their widespread use in critical applications such as hydrocarbon systems. By replacing the metallic pipes with non-metallic ones, there is a need for millions of miles of pipelines that run underground, above-the-ground, and under-the-sea, carrying everything from water to crude oil to be inspected periodically for any signs of damage that may lead to environmental disasters.

Conventional NDT methods are not suitable for the inspection of composite materials due to several reasons. The well-developed ultrasonic testing cannot be used for rubber or soft plastic. This is due to the fact that the polymers absorb nearly all ultrasound power and do not reflect the waves to be used for inspection. Furthermore, high scattering of the ultrasound waves by the mesh or fabric of a composite material causes extremely noisy reflections. In oil and gas applications, composite pipes and fittings are cured in autoclaves under atmospheric pressure which causes a relatively high percentage of voids. This, in turn, highly attenuates the ultrasonic waves, preventing the use of high-frequency ultrasonic inspections. Due to these shortcomings, the use of ultrasound NDT has led to limited success in the NDT of NMPs [9],[10]. Eddy current measurement [11], which is another common NDT method for the inspection of metallic pipes, does not work for non-conductive materials such as FRP/GRE, HDPE, and reinforced rubber components. Magnetic flux leakage measurements do not work for non-ferromagnetic materials such as FRP/GRE, HDPE, and reinforced rubber components [12]. Radiography is commonly utilized to detect changes in bulk density [13]. In some operating conditions, delamination defects in the NMP walls appear where a 2D separation occurs between adjacent component layers. This type of defect does not typically result in a detectable change in the local density and is therefore not detectable in a radiograph.

To bridge this gap, microwave NDT methods can be employed that are able to provide volumetric images of the cylindrical composite components. In these methods, data are collected over a cylindrical surface, and two-dimensional (2D) or three-dimensional (3D) images can be reconstructed using microwave imaging (MWI) techniques. During the data acquisition, scans are performed from one side of the sample much like conventional ultrasonic testing without the need for a couplant. For the inspection of pipes, the technique can be adapted to perform the scanning inside the pipes like conventional pipeline inspection gauges (PIGs) used for the NDT of the pipeline [14]. Furthermore, to expedite the imaging process, electronic scanning of antenna arrays along the azimuthal direction and mechanical scanning along the longitudinal direction have been considered, as discussed later.

MWI techniques for the inspection of NMPs can be divided into three broad categories including direct MWI (D-MWI) techniques, synthetic aperture radar-based MWI (SAR-MWI) techniques, and near-field holographic MWI (NH-MWI) techniques. The techniques in each category offer certain advantages while suffering certain drawbacks. In the following, we provide a brief review of the basics of each technique and also discuss the pros and cons associated with them.

D-MWI Using Raw Measured Data

In industry, microwave NDT technology has already been commercialized (for instance by Evisive) for the inspection of non-metallic components (e.g., see [7],[8],[15]–[17]). For this purpose, microwaves are radiated from the transducer to the component under test. Microwave energy gets scattered at every interface of changing dielectric constant. This includes the front and back surfaces of the component and every feature in the part that imposes a discontinuity in the dielectric properties (e.g., where there are delaminations, cracks, holes, impurities, or other defects). A microwave interference pattern is created due to the reflected wave combined with the transmitted wave. This interference pattern is measured with diode sensors (scalar measurements). The resulting signals are then amplified, digitized, and converted into images. The images represent the reflected microwave energy from the entire volume of the inspected material. All the defects and features along the axis orthogonal to the scanning aperture are projected on a 2D plane (2D image). Thus, the technology is not capable of resolving the features along the axis orthogonal to the measurement (scanned) aperture. For example, when inspecting multiple concentric pipes in a wellbore, it is not possible to detect which pipes are defective. Besides, the technique relies on scanning the entire domain with a single microwave transceiver.

In academia, several layered-structure inspection techniques have been developed using microwave and millimeter waves (e.g., see [18]–[20]). Although very accurate thickness estimations (in a fraction of mm range) have been provided in these works, they lack further post-processing to provide high-resolution thickness profile estimation of the pipes along the cross-range directions (azimuthal and longitudinal directions for the pipes). Furthermore, their application for cylindrical geometries such as pipes has not been discussed.

More recently, a crawling robot has been used for microwave reflectometry of NMPs [21]. Fig. 1a shows the robot which scans a microwave waveguide probe inside the pipe. The crawler is moving with two sets of wheels (each set has three wheels, and the rear set is motorized) sprung against the pipe wall. Front wheels are equipped with rotary encoders for measuring the scanned position. The probe is held on the front of the robot by a rotating clamp head which also controls its azimuthal position. The probe operates over a part of *K*-band (18–26.5 GHz) and is a flangeless open-ended waveguide that is fed by a waveguide-to-coaxial adapter. It is measured by a vector network analyzer (VNA). The HDPE pipes have been measured in three environments: 1 m of free space from the effects representing the above-ground pipelines; having an aluminum foil wrapped over the defects representing a plastic-lined metal pipe; and having salt water sealed inside the defects with plastic film and aluminum foil wrapped over, representing subsea pipelines (aluminum foil resembles salt water).

Fig. 1b shows the machined defects (notches and holes) on the outer surface of the pipe to validate the performance of the robot. Fig. 2 shows the magnitude or phase of the collected raw responses along the azimuthal (ϕ) and longitudinal (z) positions shown as 2D images. It is worth noting that in this work, the connection between the waveguide-to-coaxial adapter and VNA has been made via the use of a coaxial cable, and only 90° rotation and measurement along the azimuthal direction have been implemented around the defects' centerline. In a practical system, performing secure microwave data collection with the probe along the full 360° azimuthal direction needs to be properly addressed.

In general, while the D-MWI techniques can be made very cost-effective by performing only scalar measurements and measuring only at a single frequency or with a single antenna, they suffer certain drawbacks. They are incapable of providing radial resolution for pipe imaging since achieving radial resolution necessitates the use of additional (such as wideband) information and advanced processing techniques (such as SAR-MWI and NH-MWI, as discussed in the next sections). Instead, in D-MWI, the objects and defects at various radial positions will be projected to a 2D image plotted along the (ϕ) and (z) axes. Furthermore, since D-MWI is normally performed in the near-field of the inspected object (to achieve higher sensitivity and higher resolution benefiting from the measurement of a portion of the evanescent wave spectrum), the lateral resolution along ϕ and z is directly related to the probe's dimensions and its near-field distribution. As per [21], with a K-band waveguide, a point-wise defect typically appears with a size of 10 to 20 mm in the image.

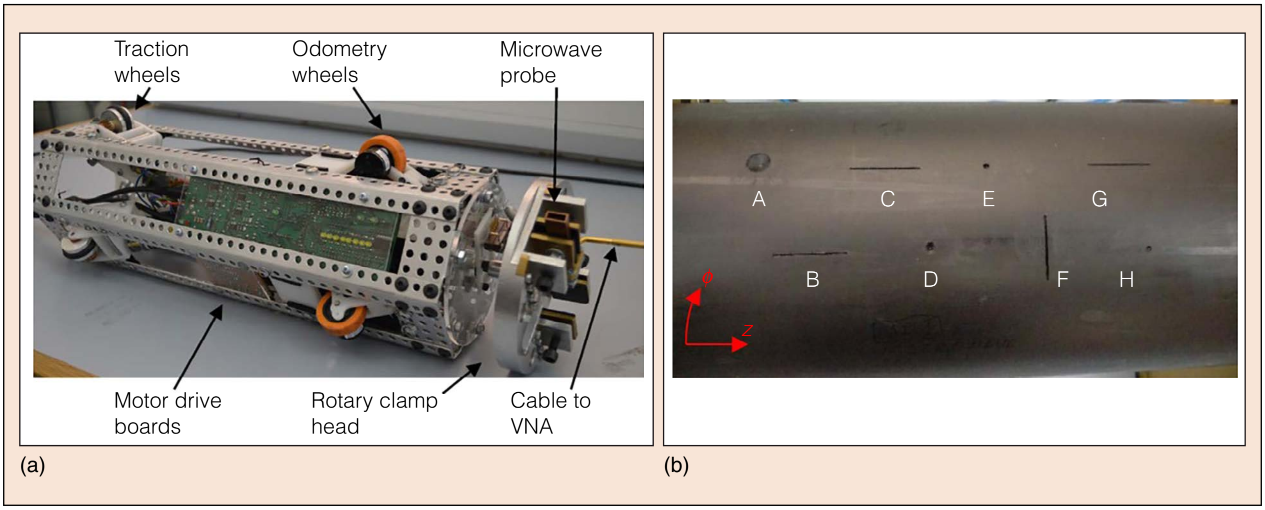

Fig. 1. (a) Pipe crawler robot with microwave waveguide attached to its rotary scanning head (b) Defects on the outer surface of the HDPE pipe (figures from [21], used with permission, ©2019 IEEE).

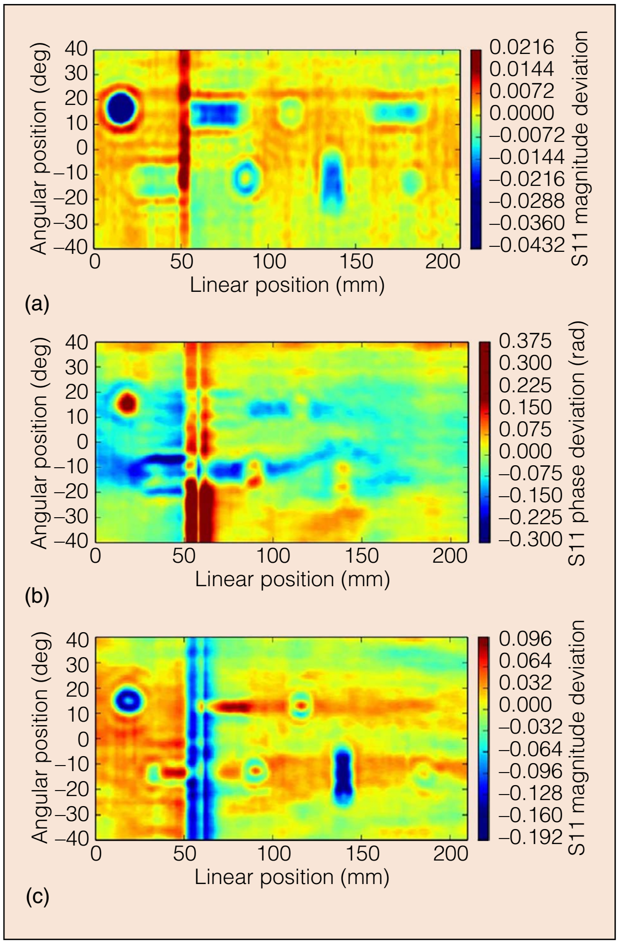

Fig. 2. Raw responses of the scanned pipe in Fig. 1b obtained from: (a) the magnitude of the reflections ($|S_{11}|$ in dB) at 19.5 GHz for the HDPE pipe without foil or salt water; (b) the phase of the reflections (phase of S_{11} in degrees) at 24 GHz for the HDPE pipe with foil and without salt water; and (c) the magnitude of the reflections ($|S_{11}|$ in dB) at 24 GHz for the HDPE pipe with foil and salt water inside the defects (figures from [21], used with permission, ©2019 IEEE).

SAR-MWI Techniques Based on Far-field Approximations

SAR-MWI techniques have been very successful in security screening using millimeter waves [22]. The main advantage of SAR-MWI is the low computational resource requirements compared to quantitative MWI techniques [23]. However, for the inspection of multilayered cylindrical structures, conventional SAR-MWI techniques that have been developed for free space cannot be employed. This is due to the additional effects of multi-layered structures such as different propagation delays (paths) for different layers, refractions, and reflections at layer boundaries. Thus, in this section, we review some of the major developments for imaging multi-layer cylindrical media using the SAR-MWI concept.

Symmetrical Structures: In [24], an X-band (8.2 GHz to 12.4 GHz) SAR-MWI has been developed for the NDT of multilayered pipes, and the image reconstruction process is based on the use of matched filters. We briefly review the basics of this technique. As shown in Fig. 3, the scattered field E^{SC} measured at the position $\boldsymbol{r}' = (\rho', \phi', z')$ due to an object with contrast function denoted by $c(\boldsymbol{r})$, where $\boldsymbol{r} = (\rho, \phi, z)$, can be written as:

$$E^{SC}(\boldsymbol{r}', \omega) = \int_V c(\boldsymbol{r}) G_{rt}(\boldsymbol{r}, \boldsymbol{r}', \omega) dv \qquad (1)$$

where V is the volume of the object and G_{rt} is the two-way Green's function which is the product of the forward and backward Green's functions [25]. This technique is based on the well-known Born approximation [26] which implies that multiple scattering inside the object is negligible. This assumption holds for small or low-contrast objects. Using the cylindrical symmetry $G_{rt}(\boldsymbol{r}, \boldsymbol{r}', \omega)$ can be written as:

$$G_{rt}(\rho', \phi', z', \rho, \phi, z, \omega) = G_{rt}(\rho', \rho, \Delta\phi, \Delta z, \omega) \qquad (2)$$

where $\Delta\phi = \phi - \phi'$ and $\Delta z = z - z'$.

Assuming that the object is only at a certain radius (negligible radial thickness) ρ_0, measurements are performed at a constant radius ρ', and using convolution theory leads to the following equation:

$$E_0^{SC}(\rho', \phi', z', \omega) = \rho_0 c(\rho_0, \phi', z') * G_{rt}(\rho', \rho_0, \phi', z', \omega) \qquad (3)$$

where E_0^{SC} is the scanned field due to a target at $\rho = \rho_0$ and $*$ denotes the covolution along ϕ and z. From (3), the contrast function $c(\rho_0, \phi', z')$ can be found using deconvolution techniques such as Wiener deconvolution [25]. The contrast function of the object can be then found as:

$$\hat{c}(\rho, \phi, z, \omega) \approx F^{-1}\left\{\tilde{E}^{SC}(\rho', k_\phi, k_z, \omega)\, \tilde{G}_{rt}^{*}(\rho', \rho, k_\phi, k_z, \omega)\right\} \qquad (4)$$

where $F\{\cdot\}$ denotes Fourier transform (FT) along ϕ and z, $\tilde{G}_{rt}(\rho', \rho, k_\phi, k_z, \omega)$ and $\tilde{E}^{SC}(\rho', k_\phi, k_z, \omega)$ are the FTs of $G_{rt}(\rho', \rho_0, \phi', z', \omega)$ and $E^{SC}(\rho', \phi', z', \omega)$, respectively, and superscript $*$ denotes the complex conjugate. It has been

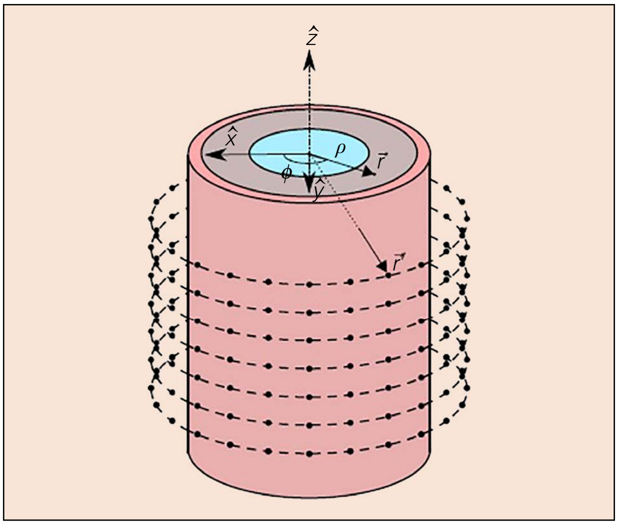

Fig. 3. Schematic of a four-layer cylindrical structure and data acquisition configuration depicting equally spaced imaging data acquisition points (from [24], used with permission, ©2019 IEEE).

suggested that the final image can be reconstructed by evaluating (4) at several observation radii between the inner and outer boundaries of the imaged cylindrical region. More specifically, it has been explained in [24] that a distributed object over several radii can be considered as a linear combination of images corresponding to the objects at each radii position, and thus (4) can be applied to reconstruct images of such objects. One issue that has been overlooked, though, is that the measured response is due to the whole distributed object, and that produces errors when it is employed to reconstruct objects at each radius separately using (4). Inspired by SAR imaging, when wideband data is available, the final contrast function $c_{final}(\boldsymbol{r})$ has been estimated as [24]:

$$c_{final}(\boldsymbol{r}) = \int_{\omega} c(\boldsymbol{r}, \omega) d\omega \tag{5}$$

To validate the performance of this imaging technique, simulation results of [24] have shown for the case that, with reference to Fig. 3, the background medium is air; the pipe is lossless with a thickness of 2 cm and $\varepsilon_r = 2$ and the medium inside the pipe has a radius of 7 cm and $\varepsilon_r = 4 - j0.01$. The data acquisition aperture has a radius of 15 cm. Since z-polarized antennas are considered, only the z-component of Green's function has been considered. Two point-wise objects are placed at the same height but at radial positions of 3 cm and 4 cm with an angular spacing of 135°. The reflection coefficient (S_{11}) has been simulated over a circular aperture for 2D imaging rather than 3D to save time. At each scanning step, 51 equally spaced frequencies are obtained in the range of 8.2–12.4 GHz (X-band). Fig. 4a and Fig. 4 b show the imaging results when using an ideal roundtrip Green's function computed from [27] and when the Green's function is obtained from numerical simulations, respectively.

Fig. 5a shows the photo of a tested PVC pipe filled with water and with internal damage hidden from the outside. An open-ended waveguide at X-band was used to collect the reflection coefficient (S_{11}) data over a cylindrical aperture using a VNA and with sampling steps of 3° and 5 mm along ϕ and z axes, respectively. Fig. 5b shows the reconstructed image using the SAR-MWI technique described above. The image is the magnitude of the reconstructed contrast function $\left|c_{final}(\boldsymbol{r})\right|$ in dB and over an inner cylinder with radius $\rho = 8$ cm which is 4 mm away from the inner pipe surface.

Symmetrical and Asymmetrical Structures: The configuration solved in the previous section had to be azimuthally symmetric. In [28], a microwave NDT process has been proposed for symmetric and asymmetric layered cylindrical lossy dielectric objects. The technique is based on the time reversal SAR imaging in X-band (8.2 – 12.4 GHz) while considering the transmission and refraction path at the boundaries between different layers. Multiple reflections have not been included in the analysis. Starting from a three-layer model shown in Fig. 6a, for a given frequency, once the number of layers of the cylindrical structure, the complex dielectric constant, radius, and axis offset of each layer are known, the transmission path is determined by minimizing the following cost function [28]:

$$F = \left(\psi_{2t}\left(\hat{\theta}_{1i}\right) - \hat{\psi}_{2t}\right)^2 + \left(\psi_{3t}\left(\hat{\theta}_{2i}\right) - \hat{\psi}_{3t}\right)^2 \tag{6}$$

where $\psi_{2t}\left(\hat{\theta}_{1i}\right)$, $\psi_{3t}\left(\hat{\theta}_{2i}\right)$, $\hat{\psi}_{2t}$, and $\hat{\psi}_{3t}$ depend on the two angles $\hat{\varphi}_2$ and $\hat{\varphi}_3$ and two height positions $\hat{z}_2$ and $\hat{z}_3$ corresponding to the positions of two transmission positions S_2 and S_3, respectively. Such dependencies for $\psi_{2t}\left(\hat{\theta}_{1i}\right)$ and $\psi_{3t}\left(\hat{\theta}_{2i}\right)$ have been derived using Snell's law of refraction. Once the real transmission positions at the boundaries between different layers

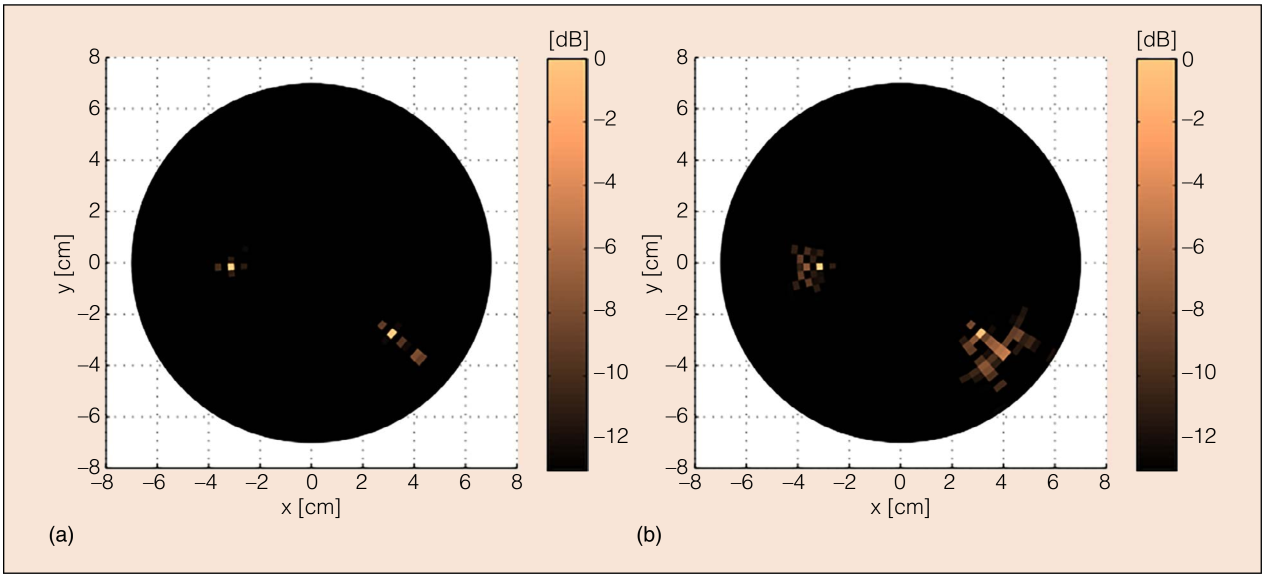

Fig. 4. Reconstructed 2D image (normalized) for two point-wise objects at radial positions of 3 cm and 4 cm with an angular spacing of 135°, when using SAR-MWI for symmetrical structures and with: (a) with ideal roundtrip Green's function; and (b) full-wave simulation of a finite cylinder (figures from [24], used with permission, ©2019 IEEE).

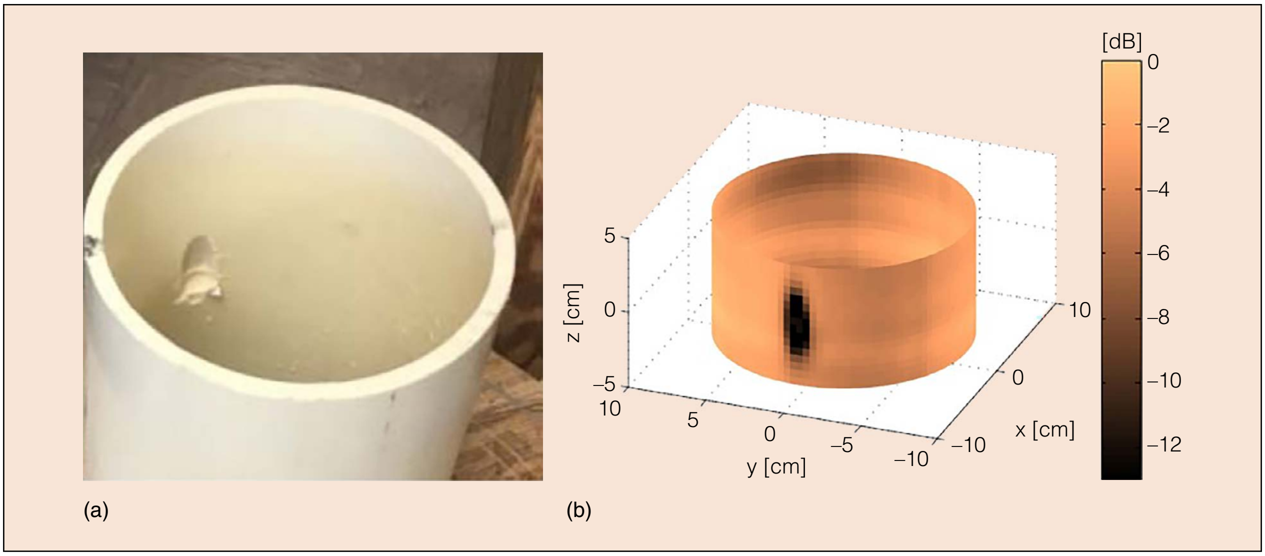

Fig. 5. (a) PVC pipe with internal damage; (b) The corresponding estimated normalized contrast function ($|c_{final}(r)|$) at $\rho = 8$ cm when using SAR-MWI for symmetrical structures (figures from [24], used with permission, ©2019 IEEE).

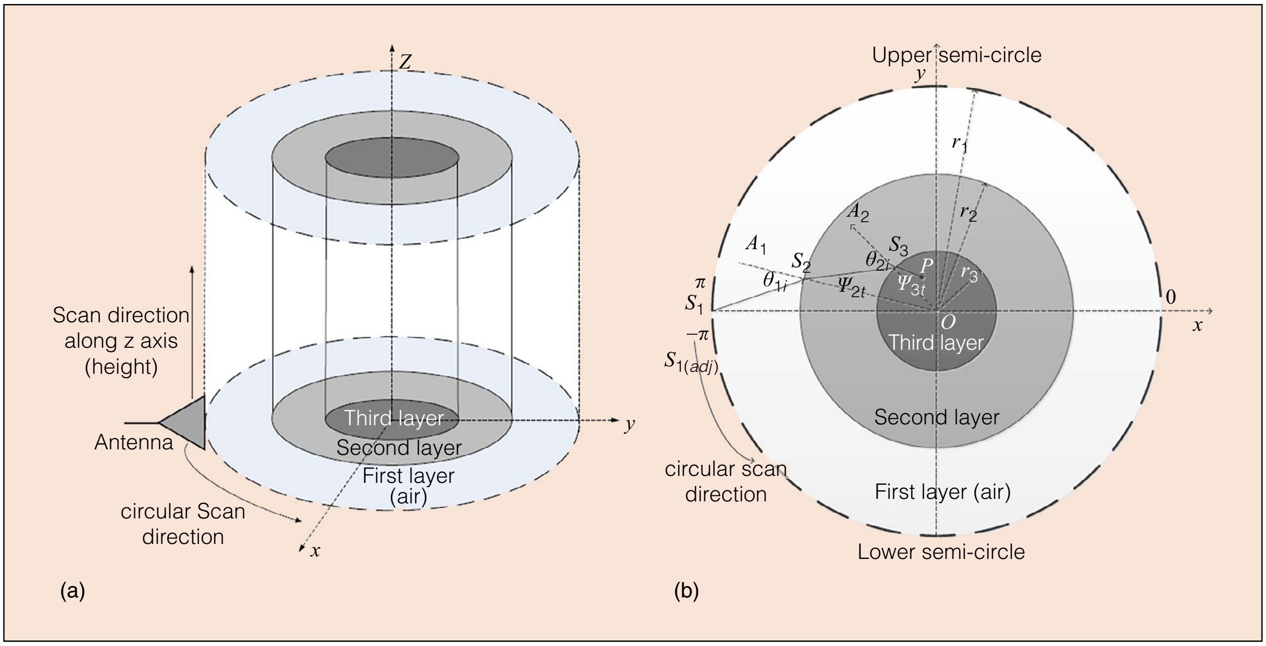

Fig. 6. (a) A lossy three-layer cylindrical structure showing two scan directions in cylindrical SAR-MWI; (b) A circular slice of the cylindrical structure (figures from [28], used with permission, ©2019 IEEE).

namely $S_{2(est)}$ and $S_{3(est)}$ are determined by minimizing the cost function (6) with respect to four parameters $\hat{\varphi}_2$, $\hat{\varphi}_3$, $\hat{z}_2$, and $\hat{z}_3$, the two-way transmission coefficients at the boundary of the m-th and n-th layers can be written as [28]:

$$\tau_{mn\perp(round)} = (2\eta_n cos\theta_{mi} 2\eta_m cos\theta_{nt}) / (\eta_n cos\theta_{mi} + \eta_m cos\theta_{nt})^2 \quad (7)$$

$$\tau_{mn\|(round)} = (2\eta_n cos\theta_{mi} 2\eta_m cos\theta_{nt}) / (\eta_n cos\theta_{nt} + \eta_m cos\theta_{mi})^2 \quad (8)$$

where "⊥" and "‖" denote the perpendicular and parallel polarizations, η_m is the intrinsic impedance of any given m-th layer, and $cos\theta_{mi}$ and $cos\theta_{nt}$ are found using the Snell's law of refraction as described in [29].

Using the transmission coefficients derived above, if the transmitted signal at the point S_1 is denoted by E and the reflected signal at point P is denoted by P_r, the received signal at S_1 due to the object at P can be written as [28]:

$$S_{1P(rec)\perp} = E_\perp P_{\perp r} \tau_{12\perp(round)} \tau_{23\perp(round)} \times exp\left(-j2(k_1 |\overrightarrow{S_1S_2}| + k_2 |\overrightarrow{S_2S_3}| + k_3 |\overrightarrow{S_3P}|)\right) \quad (9)$$

$$S_{1P(rec)\|} = E_\| P_{\|r} \tau_{12\|(round)} \tau_{23\|(round)} \times exp\left(-j2(k_1 |\overrightarrow{S_1S_2}| + k_2 |\overrightarrow{S_2S_3}| + k_3 |\overrightarrow{S_3P}|)\right) \quad (10)$$

where $|\vec{A}|$ is the magnitude of any vector A and k_m is the wavenumber of any given layer m.

The received signal at the point S_1 for an N-layer structure can be obtained similarly. For an object located in the N-th layer (the innermost layer), the optimization problem needs to be solved for 2×(N-1) parameters for a cylindrical imaging system. If $l_{1(rec)\perp}$ and $l_{1(rec)\|}$ are defined as below [28]:

$$l_{1(rec)\perp} = \mathrm{P}_{\perp r}\tau_{12\perp(round)}\tau_{23\perp(round)}\cdots\tau_{N-1N\perp(round)} \times exp\left(-j2(k_1|\overrightarrow{S_1S_2}|+\cdots+k_N|\overrightarrow{S_NP}|)\right) \tag{11}$$

$$l_{1(rec)\|} = \mathrm{P}_{\|r}\tau_{12\|(round)}\tau_{23\|(round)}\cdots\tau_{N-1N\|(round)} \times exp\left(-j2(k_1)|\overrightarrow{S_1S_2}|+\cdots+k_N|\overrightarrow{S_NP}|\right) \tag{12}$$

then, the received signal at the point S_1 from the object at point P for an N-layer structure can be written as [28]:

$$\left[S_{1P(rec)\perp}, S_{1P(rec)\|}\right] = \begin{bmatrix} a_{\perp\perp}E_\perp & a_{\perp\|}E_\perp \\ a_{\|\perp}E_\| & a_{\|\|}E_\| \end{bmatrix} \begin{bmatrix} l_{1(rec)\perp} \\ l_{1(rec)\|} \end{bmatrix} \tag{13}$$

where a is a real number and is the decomposed coefficient along the parallel and perpendicular directions.

Using the modeled received signal at any measurement point S_1 for any object at point P, using SAR imaging concepts, the image of the inspected domain c can be reconstructed as [28]:

$$c(x_i,y_j,z_k) = \sum_{Z_{meas}}\sum_{\phi_1} S_{1(rec)}(Z_{meas},\phi_1)S^*_{1ref}(x_i,y_j,z_k,Z_{meas},\phi_1) \tag{14}$$

where (x_i,y_j,z_k) represent the coordinates of the imaged object, ϕ_1 is the aspect angle of the measurement points, Z_{meas} represents the height of the measurement points, and $S_{1ref}(x_i,y_j,z_k,Z_{meas},\phi_1)$ denotes the reference signal with respect to the variables x_i, y_j, z_k, ϕ_1 and Z_{meas}.

Fig. 7a shows an HDPE pipe with two screws before being filled with dry and fine sand [28]. An open-ended waveguide at X-band (8.2–12.4 GHz) and a VNA were used to measure the reflection coefficient S_{11} over a cylindrical aperture with radius of 250 mm. Measurements were carried out at 101 frequencies within that band and the sampling steps along the ϕ and z axes were 3° and 5 mm, respectively. The HDPE pipe had a thickness of 20 mm and inner radius of 73 mm. With reference to Fig. 6, this is a three-layer structure with the first, second, and third layers being air, HDPE pipe, and sand, respectively. The complex relative permittivity of the HDPE pipe and sand are $\varepsilon_r = 2.2 - j0$ and $\varepsilon_r = 2.6 - j0.3$, respectively. After applying the described imaging method, the reconstructed 3D image ($|c(x,y,z)|$ obtained from (14)) is shown in Fig. 7b [28] which clearly shows the presence and

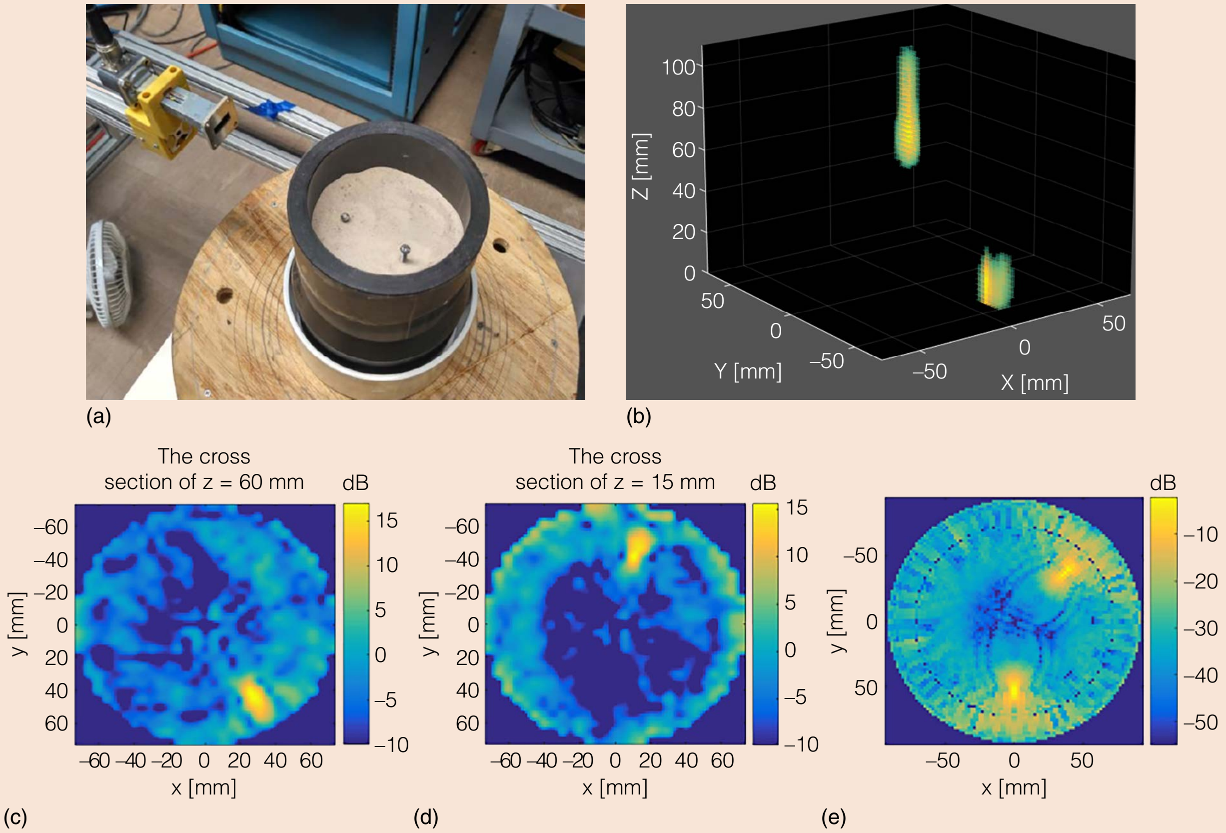

Fig. 7. (a) HDPE pipe with two screws before being completely filled by sand; (b) 3D SAR image of two screws when using the imaging technique; (c) 2D image at the cross-section of z = 60 mm; (d) 2D image at the cross-section of z = 15 mm; (e) 2D image when using the simulated data with the same parameters as those used in the real experiment (figures from [28], used with permission, ©2019 IEEE).

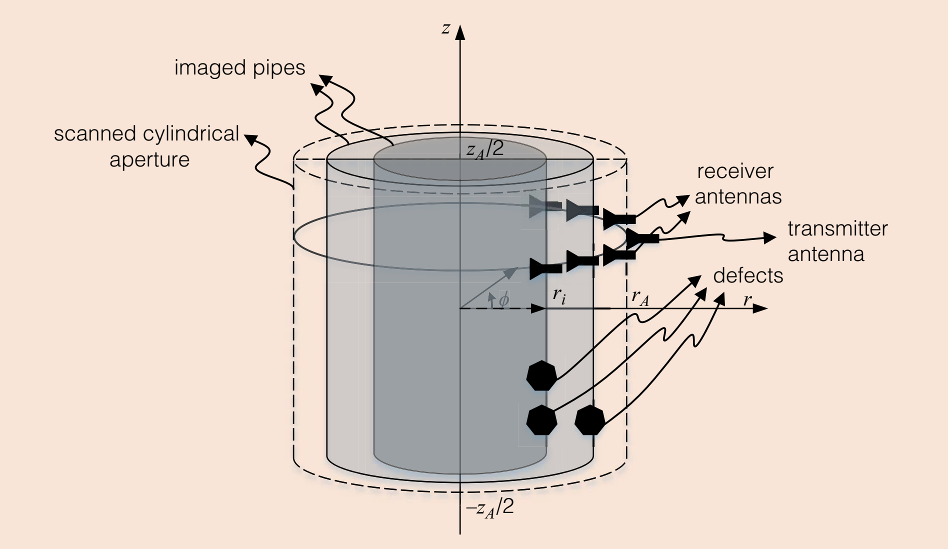

Fig. 8. Illustration of the NH-MWI setup. A transmitter antenna and N_A receiver antennas scan a cylindrical surface and the images are reconstructed over NMPs with radii $r = r_i$ (from [31], used with permission, ©2020 IEEE).

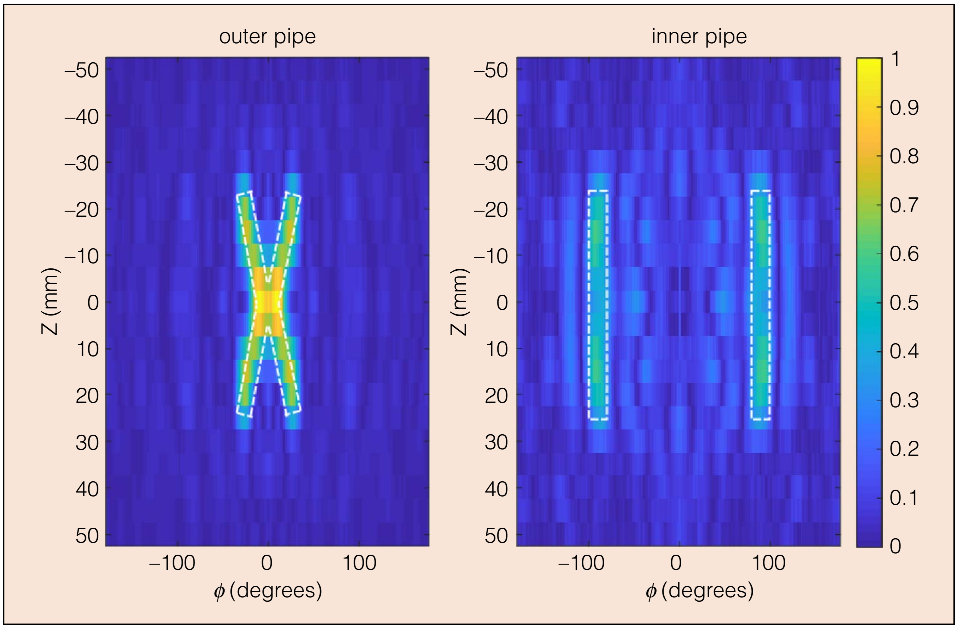

Fig. 9. Reconstructed images when using NH-MWI technique, where the white dashed lines show the true boundaries of the defects (from [31], used with permission, ©2020 IEEE).

shape of the screws. Furthermore, Fig. 7c and Fig. 7d show the 2D cross-section images at z positions of 60 mm and 15 mm, respectively. These images also show the correct locations of the two screws [28].

To validate the results obtained from the experimental setup, the same parameters were employed to provide simulation data for imaging (except that the screws are placed at the same height to save the simulation time). After applying the imaging technique to the simulation data, Fig. 7e shows the 2D cross-section image (passing through the two screws) which closely matches the experimental imaging results for the screws in Fig. 7c and Fig. 7d [28].

While SAR-MWI techniques are fast and capable of providing radial resolution in pipe imaging, their main drawbacks are that: they assume point-wise antennas which ignores the near-field distribution of the antennas in near-field imaging; and they assume pre-known values for the wavenumbers of the imaged layers which may not be sufficiently accurate in a practical system.

NH-MWI Techniques Adapted for Extreme Near-field Applications

Here, we briefly review the theory of NH-MWI [30] with an array of receiver antennas and multiple frequency data for imaging the defects in concentric NMPs. In this imaging problem, the collected data are functions of azimuthal and longitudinal spatial variables and the reconstructed images are also versus similar variables but at different radial positions. Thus, the functions representing the acquired data and the reconstructed images are periodic with respect to the azimuthal spatial variable (ϕ). To process the data using Fourier Transform (FT) as discussed later, the circular convolution concept will be utilized.

Fig. 8 shows the microwave NMP imaging setup. It includes one transmitter antenna that produces the illuminated microwave power for the inspection of the NMPs and N_A receiver antennas that are placed on both sides of the transmitter antenna to measure the scattered fields from the NMPs [31]. For performing imaging, the transmitter and receiver antennas move together and scan a cylindrical surface (aperture) with the radius and height of r_A and z_A, respectively. The scattered fields are measured at N_ϕ angles and N_z positions along the azimuthal (ϕ) (within $[0, 2\pi]$) and longitudinal z directions, respectively. For each sampling position, the scattered field denoted by $E^{SC}(\phi, z)$ is

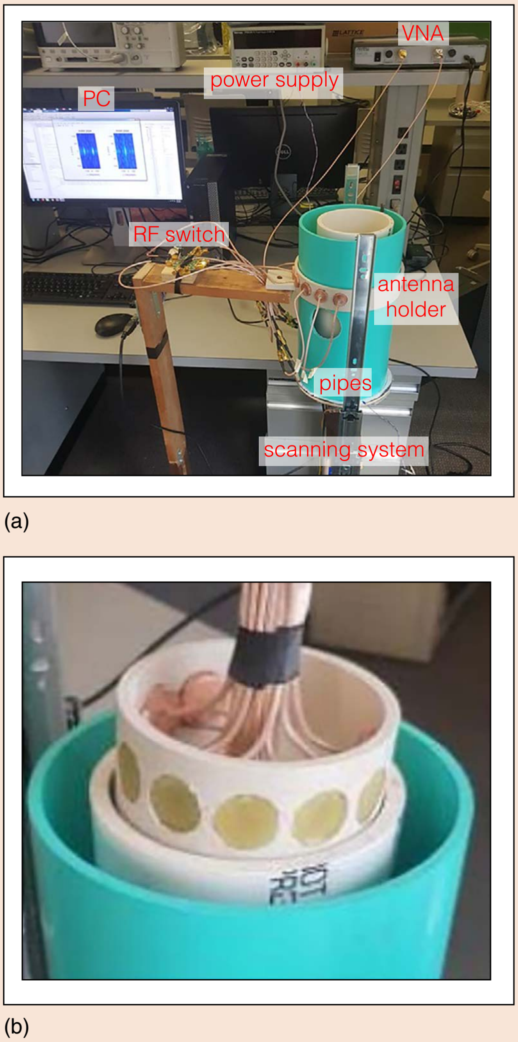

Fig. 10. Experimental setup for NH-MWI with an antenna array scanning the pipes from: (a) outside; and (b) inside the pipes (from [31], used with permission, ©2020 IEEE).

acquired at N_ω frequencies in the range of ω_1 to ω_{N_ω}, by each receiver antenna. The goal of this imaging procedure is to produce images of N_r NMPs with radii r_i, $i = 1,\ldots,N_r$. In the NH-MWI process, we assume that the imaging system is linear and space-invariant (LSI). The linear property of the system is based on the Born approximation which supposes that the defects are small or low-contrast with respect to the background medium (NMP) [26]. Also, the space-invariant property of the system indicates that if the defect is shifted along the azimuthal or longitudinal directions, the response of that shifts with the same amount and along the same direction. This implies that the pipes are uniform around the azimuthal direction and sufficiently long along the longitudinal direction such that the edge effects can be neglected.

For the implementation of NH-MWI, first, the point-spread functions (PSFs) of the LSI imaging system are acquired. These PSFs denoted by $E^{SC,CD}$ are approximated by measuring the responses for small defects, called calibration defects (CDs), which are placed at the origin of the ϕ and z axes, on each NMP and one at a time. The scattered response that is acquired for a CD on the i-th NMP is denoted by $E_i^{SC,CD}(\phi,z)$. Then, using the convolution theory, the response of the tested NMPs denoted by $E_i^{SC}(\phi,z)$ is written as the convolution of the *a priori* measured PSF for that NMP, $E_i^{SC,CD}(\phi,z)$, with the defect's contrast function for the corresponding NMP $c_i(\phi,z)$. By using this signal modelling for each NMP, then, the total response measured for all NMPs, $E^{SC}(\phi,z)$, is written as the superposition of the responses for all NMPs, $E_i^{SC}(\phi,z), i = 1,\ldots,N_r$, as:

$$E^{SC}(\phi,z) = \sum_{i=1}^{N_r} E_i^{SC}(\phi,z) = \sum_{i=1}^{N_r} E_i^{SC,CD}(\phi,z) *_\phi *_z c_i(\phi,z) \quad (15)$$

where $*_\phi$ and $*_z$ denote the convolutions along ϕ and z, respectively. In (15), PSF functions are acquired beforehand via measurement or simulation and they are assumed to be known. Also, $E^{SC}(\phi,z)$ is obtained by measuring the responses for the defects on the NMPs. The goal is then to compute the defect's contrast functions $c_i(\phi,z)$. It can be seen that in (15), there are N_r unknowns $(c_i(\phi,z), i = 1,\ldots,N_r)$ to be solved. Thus, one equation is not sufficient for this purpose. To be able to solve this problem, measurements need to be performed at several frequencies, ω_n, n=1,…,N_ω and/or by several receivers, a_m, m=1,…,N_A. For instance, for every receiver with an index a_m, (15) can be written for several frequencies leading to the following system of equations:

$$\begin{cases} E_{a_m}^{SC}(\phi,z,\omega_1) = \sum_{i=1}^{N_r} E_{i,a_m}^{SC,CD}(\phi,z,\omega_1) *_\phi *_z c_i(\phi,z) \\ \vdots \\ E_{a_m}^{SC}(\phi,z,\omega_{N_\omega}) = \sum_{i=1}^{N_r} E_{i,a_m}^{SC,CD}(\phi,z,\omega_{N_\omega}) *_\phi *_z c_i(\phi,z) \end{cases} \quad (16)$$

The systems of equations that are generated for all the receiver antennas a_m, m=1,…,N_A, can be combined in a single larger system of equations to compute the unknown parameters $c_i(\phi,z), i = 1,\ldots,N_r$, which are shared between all the systems of equations. For solving each system of equations, Fourier Transform (FT) is applied on both sides of the equations.

Applying discrete FT (DFT) and discrete-time FT (DTFT) along the ϕ and z axes, respectively, leads to the following system of equations at each spatial frequency pair $\boldsymbol{\kappa} = (k_\phi, k_z)$:

$$\underline{\tilde{\tilde{\boldsymbol{E}}}}^{SC} = \underline{\underline{\tilde{\tilde{\boldsymbol{D}}}}}\,\underline{\tilde{\tilde{\boldsymbol{C}}}} \quad (17)$$

where

$$\underline{\tilde{\tilde{\boldsymbol{E}}}}^{SC} = \begin{bmatrix} \underline{\tilde{\tilde{E}}}_1^{SC} \\ \vdots \\ \underline{\tilde{\tilde{E}}}_{N_A}^{SC} \end{bmatrix}, \quad \underline{\underline{\tilde{\tilde{\boldsymbol{D}}}}} = \begin{bmatrix} \underline{\underline{\tilde{\tilde{D}}}}_1 \\ \vdots \\ \underline{\underline{\tilde{\tilde{D}}}}_{N_A} \end{bmatrix}, \quad \underline{\tilde{\tilde{\boldsymbol{C}}}} = \begin{bmatrix} \tilde{\tilde{c}}_1(\boldsymbol{\kappa}) \\ \vdots \\ \tilde{\tilde{c}}_{N_r}(\boldsymbol{\kappa}) \end{bmatrix},$$

$$\underline{\tilde{\tilde{E}}}_{a_m}^{SC} = \begin{bmatrix} \tilde{\tilde{E}}_{a_m}^{SC}(\boldsymbol{\kappa},\omega_1) \\ \vdots \\ \tilde{\tilde{E}}_{a_m}^{SC}(\boldsymbol{\kappa},\omega_{N_\omega}) \end{bmatrix}, \text{ and}$$

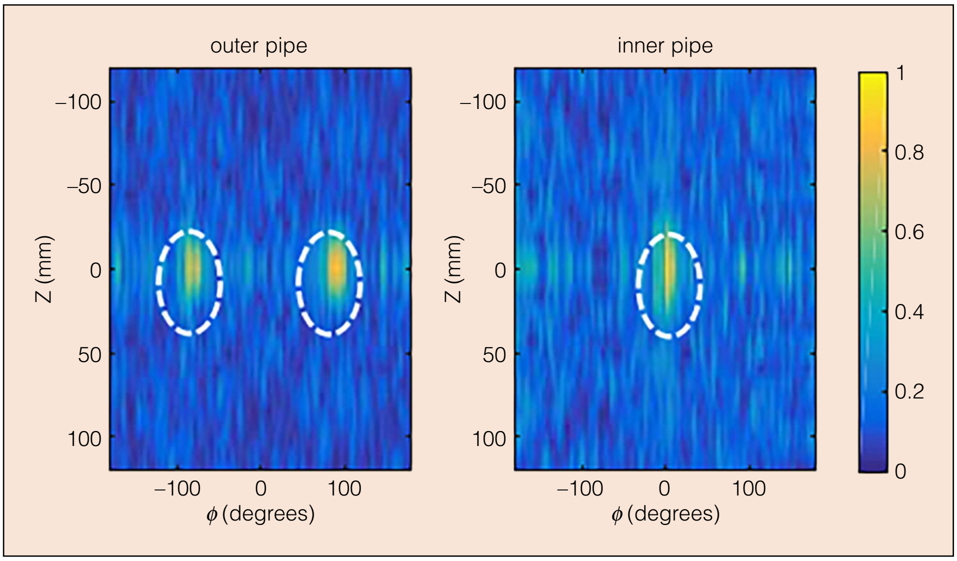

Fig. 11. Reconstructed images of the inner and outer pipes using experimental data collected by eight receiver antennas scanning the pipes from outside when using NH-MWI augmented with the standardized minimum norm and with using the data at 10 frequencies within the band of 6 to 8 GHz. White dashed lines show the true boundaries of the defects (from [31], used with permission, ©2020 IEEE).

$$\underline{\underline{\tilde{\tilde{\boldsymbol{D}}}}}_{a_m} = \begin{bmatrix} \tilde{\tilde{\boldsymbol{E}}}^{SC,CD}_{1,a_m}(\boldsymbol{\kappa},\omega_1) & \cdots & \tilde{\tilde{\boldsymbol{E}}}^{SC,CD}_{N_r,a_m}(\boldsymbol{\kappa},\omega_1) \\ \vdots & \ddots & \vdots \\ \tilde{\tilde{\boldsymbol{E}}}^{SC,CD}_{1,a_m}(\boldsymbol{\kappa},\omega_{N_\omega}) & \cdots & \tilde{\tilde{\boldsymbol{E}}}^{SC,CD}_{N_r,a_m}(\boldsymbol{\kappa},\omega_{N_\omega}) \end{bmatrix}$$

After solving the systems of equations at all spatial frequency pairs $\boldsymbol{\kappa} = (k_\phi, k_z)$, the contrast function of the defects $\tilde{\tilde{c}}_i(\boldsymbol{\kappa})$, $i = 1, \ldots, N_r$, will be obtained in the spectral domain. In the next step, inverse DTFT along z and inverse DFT along ϕ are applied to $\tilde{\tilde{c}}_i(\boldsymbol{\kappa})$ to reconstruct an image $c_i(n_\phi, n_z)$ over each NMP. For the visualization of the results, the normalized image $|c_i(n_\phi, n_z)|/M$, where $|a|$ is the absolute value of a and M is the maximum of $|c_i(n_\phi, n_z)|$ for all the images, is plotted versus the spatial variables ϕ and z. This provides a 2D image of the defects on each NMP.

Recently, two techniques have been proposed to effectively improve the solution of the system of (17) using the standardized minimum norm approach [31] and the beamspace transformation approach [32]. To achieve range (radial) resolution, in [31], an array of receiver antennas has been employed along with data collection at a narrow band (6 – 8 GHz).

Here, we show the performance of the imaging technique in [31] using simulation data. Two concentric PVC pipes with outer diameters of 40 mm and 20 mm and thicknesses of 2 mm are scanned by 13 z-polarized dipole antennas over a cylindrical aperture with a radius of 50 mm and a height of 100 mm. The sampling steps along the ϕ and z axes are 2° and 5 mm, respectively. The center antenna acts as the transmitter while all the other antennas act as receivers. The angular separation between the antennas is 10°. Fig. 9 shows the reconstructed images in which the boundaries of the defects are shown by white dashed lines [31]. It is observed that the NH-MWI can accurately reconstruct the shape of the defects.

Fig. 10 shows two versions of the NDT tool developed in [31] to scan the pipes from the outside and the inside, and Fig. 11 shows the imaging results for the former tool. Overall, it was demonstrated that the tool scanning the pipes from the outside provides more satisfactory results due to the larger angular separation between the antennas leading to gathering more diverse information. In [32], a single antenna acted as both transmitter and receiver collecting wideband data (6 – 14 GHz). With this information, defects on double concentric PVC pipes (similar to [31]) have been imaged successfully.

In [31], it was found that the use of an array of receiver antennas scanning the NMPs together with the transmitter antenna and processing the responses with the NH-MWI algorithm provides excellent radial (range) resolution. This is due to the use of evanescent waves in this near-field microwave imaging technique that leads to resolutions beyond the diffraction limit. Thus, in [33], this property of such an imaging approach has been employed to perform a quantitative assessment of the thickness of a thick NMP. There, this was demonstrated for thickness estimation along the azimuthal direction. To do that, first, 1D images (along ϕ) $c_i(n_\phi)$ are produced using the approach discussed above for several imaged circles within the confines of the NMP's wall. Then, these 1D images are employed to obtain the thickness of the NMP at each ϕ position $T(n_\phi)$ [33] as:

$$T(n_\phi) = T_P \left(1 - \frac{1}{N_r} \sum_{i=1}^{N_r} \frac{|c_i(n_\phi)|}{M}\right) \tag{18}$$

where T_P is the nominal thickness of the NMP. In this approach, the normalized images of the defect on all the imaged circles are added together to obtain the overall thickness of the NMP (after proper scaling of the results as shown in (18)). The larger the defect is along the radial direction, the larger the number of the imaged circles would be that contain the effect of that defect. According to (18), this leads to a larger deviation from the nominal thickness. Furthermore, in [33], a technique has been proposed to identify the type of liquid carried inside the pipe. This further improves the accuracy of the thickness evaluation process.

Fig. 12a shows the NH-MWI system for thickness estimation of a two-layer pipe. The two-layer pipe (zoomed top view shown in Fig. 12b includes an outer layer (shown in black) made of HDPE pipe and an inner one (shown in yellow) which

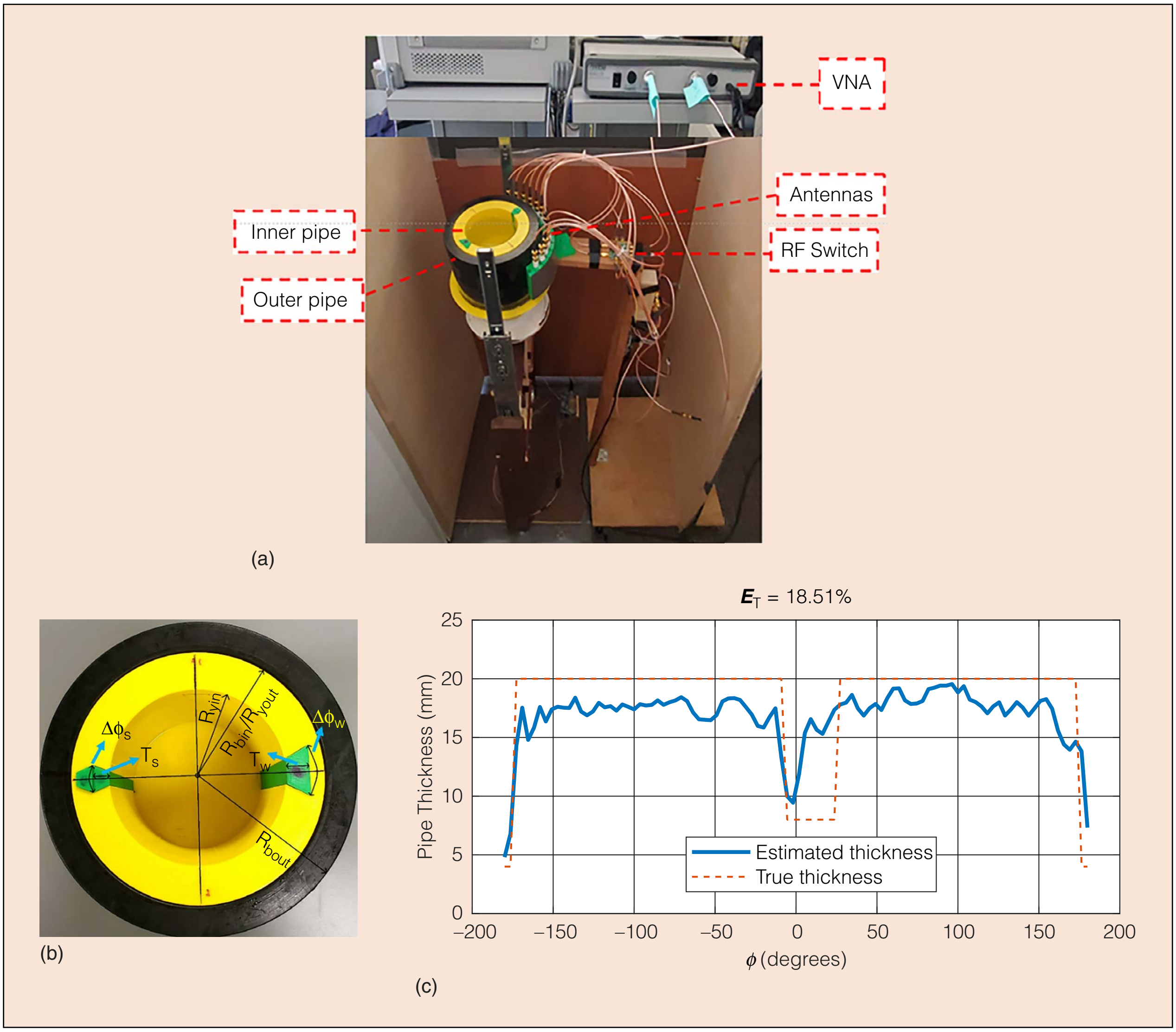

Fig. 12. (a) Experimental setup for thickness estimation of inner pipe in a two-layer pipe configuration; (b) Fabricated two-layer pipe including an HDPE layer (black), 3D printed layer (yellow), and 3D printed retractable pieces to create CDs and tested defects (green); and (c) the estimated thickness profile for the inner layer compared with the true thickness profile (from [33], used with permission, ©2022 IEEE).

is a 3D printed layer with 3D printed retractable pieces (shown in green) for creating a test defect and CDs in the lab. The pipe is filled with water. An array of 13 commercial dipole antennas has been employed to measure responses at 10 frequencies over 5.5 – 6.5 GHz band. The center antenna acts as the transmitter while all the other antennas act as receivers, collecting the data over a circular aperture every 3.6°. The transmission scattering parameters at each scanning position are measured with the aid of a microcontroller, an RF switch, and a VNA. Two levels of thickness estimation are performed for the inner layer (3D printed layer) by measuring two PSFs for that. For this purpose, each time, one of the small retractable green pieces on the left side of Fig. 12b is removed, creating a CD at that certain radial position, and the corresponding PSF is measured over the aperture. Then, the large retractable green piece on the right side of Fig. 12b is removed, creating a defect. To reconstruct the thickness profile, the NH-MWI is first applied to obtain images of the contrast function $c_i\left(n_\phi\right)$ over two circles on the yellow pipe. Then, (18) is used to estimate the thickness profile of the yellow layer, as shown in Fig. 12c. The comparison with the true thickness profile in this figure confirms the high accuracy of this pipe thickness estimation technique.

While the NH-MWI techniques can be more accurate and provide higher resolution results due to the processing of measured evanescent wave spectrum, they suffer some other drawbacks such as high sensitivity to the stand-off distance of the sensor (separation between the antenna and the component surface) and the requirement for prior measurement of PSF data.

Conclusions

The growth of using NMPs to replace metallic pipes necessitates the development of NDT systems that can provide fast and robust inspection of hundreds of miles of pipelines.

In this article, we reviewed the recent progress on microwave NDT of NMPs which can address this pressing need. We reviewed the data acquisition schemes and processing algorithms for three groups of relevant techniques along with their advantages and disadvantages. The recent progress in the processing algorithm has resonated well with the progress in the development of cost-effective and compact microwave and millimeter wave data acquisition circuitry (e.g., see [34]). While microwave NDT of NMPs is a relatively new technique that still needs further development and optimization, it is expected to be widely used for the inspection of the nonmetallic pipeline due to the advantages of being safe, capable of imaging multiple concentric pipes, and contactless (no need for any couplant). While the processing algorithms are fast, the data acquisition by mechanical scanning of the antennas renders the whole microwave NDT slow. To tackle this problem, the use of antenna arrays along the azimuthal direction has been proposed (e.g., see [35]) which reduces the scan time and also errors due to the mechanical ripples of the sensor during the scanning procedure. Other challenges to be resolved, either via appropriate processing or hardware developments, include the high sensitivity of the results to the stand-off distance of the antenna from the surface of the imaged component and also the interfering effect of objects surrounding the pipes. While imaging defects are the main focus of microwave NDT, other new applications can be developed as well such as the detection and evaluation of the eccentricity of multiple pipes [36].

Acknowledgment

This work was supported by the U.S. National Science Foundation (NSF) under Award 1920098 and a New York Institute of Technology's ISRC grant.

References

[1] T. A. Sebaey, "Design of oil and gas composite pipes for energy production," *Energy Procedia*, vol. 162, pp. 146–155, 2019.

[2] R. K. Krishnaswamy, "Analysis of ductile and brittle failures from creep rupture testing of high-density polyethylene (HDPE) pipes," *Polymer*, vol. 46, no. 25, pp. 11664–11672, 2005.

[3] F. Saghir, S. Gohari, F. Mozafari, N. Moslemi, C. Burvill, A. Smith, and S. Lucas, "Mechanical characterization of particulated FRP composite pipes: a comprehensive experimental study," *Polymer Testing*, vol. 93, no. 107001, 2021.

[4] S. Kharkovsky and R. Zoughi, "Microwave and millimeter wave nondestructive testing and evaluation - overview and recent advances," *IEEE Instrum. Meas. Mag.*, vol. 10, no. 2, pp. 26–38, Apr. 2007.

[5] M. T. Ghasr, K. Ying, and R. Zoughi, "3D millimeter wave imaging of vertical cracks and its application for the inspection of HDPE pipes," *AIP Conf. Proc.*, vol. 1581, no. 1, pp. 1531–1536, 2014.

[6] M. A. Parvez, A. Y. Asiri, A Badghaish, A. K. Al-Dossary, and A. Al-Mehlisi, "Saudi Aramco details nonmetallic products deployment in oil, gas," *Oil and Gas J.*, 2018.

[7] R. Stakenborghs, "Microwave inspection method and its application to FRP," in *Proc. MTI AmeriTAC 110 Conf.*, 2013.

[8] R. Stakenborghs, "Microwave based NDE inspection of HDPE pipe welds," in *Proc. of 17th Int. Conf. Nuclear Engin. (ICONE17)*, 2009.

[9] K. Murphy and D. Lowe, "Evaluation of a novel microwave based NDT inspection method for polyethylene joints," in *Proc. ASME Pressure Vessels Piping Conf.*, pp. 321–327, 2011.

[10] X. W. Zhu, J. P. Pan, and L. J. Tan, "Microwave scan inspection of HDPE piping thermal fusion welds for lack of fusion defect," *Appl. Mech. Mater.*, vols. 333–335, pp. 1523–1528, Jul. 2013.

[11] L. E. S. Martin, A. E. Fouda, R. K. Amineh, I. Capoglu, B. Donderici, S. S. Roy, and F. Hill, "New high-definition frequency tool for tubing and multiple casing corrosion detection," in *Proc. SPE Abu Dhabi Int. Petroleum Exhibition & Conf.*, 2017.

[12] R. K. Amineh, N. K. Nikolova, J. P. Reilly, and J. R. Hare, "Characterization of surface breaking cracks using one tangential component of magnetic leakage field," *IEEE Trans. Magnetics*, vol. 44, no. 4, pp. 516–524, 2008.

[13] M. Tanvi and K. Manish, "Review on radiographic imaging modalities for non-destructive testing and evaluation (NDT & E)," in *Proc. Int. Conf. on Sustainable Computing in Sci., Technol. Management (SUSCOM)*, 2019.

[14] J. Quarini and S. Shire, "A review of fluid-driven pipeline pigs and their applications," *Proceedings of the Institution of Mechanical Engineers, Part E: Journal of Process Mechanical Engineering*, vol. 221, no. 1, pp. 1–10, 2007.

[15] Evisive LLC, https://evisive.com/

[16] K. Schmidt, T. Aljundi, G. A. Subaii, and J. Little, "Microwave interference scanning inspection of nonmetallic pipes," in *Proc. 5th Middle East Nondestructive Testing Conf. & Exhibition*, 2009.

[17] D. M. Tripathi, S. Gunasekaran, S. S. Murugan, and N. A. Enezi, "NDT by microwave test method for non metallic component," in *Proc. Indian National Seminar & Exhibition on Non-Destructive Evaluation NDE*, 2016.

[18] R. Zoughi and S. Ganchev, "Microwave nondestructive evaluation, state-of-the-art review," *Nondestructive Testing Information Analysis Center (NTIAC)*, Texas Research Institute Austin, Inc., Austin, Texas, USA, Feb. 1995.

[19] R. Felbecker, W. Keusgen, A. Kortke, and M. Peter, "Estimation of effective permittivity and effective thickness of inhomogeneous materials at 52–70 GHz," in *Proc. 3rd European Conf. on Antennas and Propag. (EuCAP)*, 2009.

[20] M. T. Ghasr, D. Simms, and R. Zoughi, "Multimodal solution for a waveguide radiating into multilayered structures—dielectric property and thickness evaluation," *IEEE Trans. Instrum. Meas.*, vol. 58, no. 5, pp. 1505–1513, May 2009.

[21] T. D. Carrigan, B. E. Forrest, H. N. Andem, K. Gui, L. Johnson, J. E. Hibbert, B. Lennox, and R. Sloan, "Nondestructive testing of nonmetallic pipelines using microwave reflectometry on an in-line inspection robot," *IEEE Trans. Instrum. Meas.*, vol. 68, no. 2, pp. 586–594, Feb. 2019.

[22] D. M. Sheen, D. L. McMakin, and T. E. Hall, "Three-dimensional millimeter-wave imaging for concealed weapon detection,"

IEEE Trans. Microwave Theory and Techniques, vol. 49, no. 9, pp. 1581–1592, Sep. 2001.

[23] N. K. Nikolova, *Introduction to Microwave Imaging.* Cambridge, U.K.: Springer, 2017.

[24] J. Laviada, B. Wu, M. T. Ghasr, and R. Zoughi, "Nondestructive evaluation of microwave-penetrable pipes by synthetic aperture imaging enhanced by full-wave field propagation model," *IEEE Trans. Instrum. Meas.*, vol. 68, no. 4, pp. 1112–1119, Apr. 2019.

[25] M. Fallahpour, J. T. Case, M. T. Ghasr, and R. Zoughi, "Piecewise and Wiener filter-based SAR techniques for monostatic microwave imaging of layered structures," *IEEE Trans. Antennas Propag.*, vol. 62, no. 1, pp. 282–294, Jan. 2014.

[26] M. Pastorino, *Microwave Imaging.* Hoboken, New Jersey, USA: Wiley, 2010.

[27] L.-W. Li, M.-S. Leong, T.-S. Yeo, and P.-S. Kooi, "Electromagnetic dyadic Green's functions in spectral domain for multilayered cylinders," *J. Electromagn. Waves Appl.*, vol. 14, no. 7, pp. 961–985, 2000.

[28] B. Wu, Y. Gao, J. Laviada, M. T. Ghasr, and R. Zoughi, "Time-reversal SAR imaging for nondestructive testing of circular and cylindrical multi-layered dielectric structures," *IEEE Trans. Instrum. Meas*, vol. 69, no. 5, pp. 2057–2066, May 2019.

[29] C. A. Balanis, *Advanced Engineering Electromagnetics.* Hoboken, New Jersey, USA: John Wiley & Sons, 1999.

[30] R. K. Amineh, N. K. Nikolova, and M. Ravan, *Real-Time Three-Dimensional Imaging of Dielectric Bodies Using Microwave/Millimeter Wave Holography.* Piscataway, New Jersey, USA: Wiley & IEEE Press, 2019.

[31] H. Wu, M. Ravan, R. Sharma, J. Patel, and R. K. Amineh, "Microwave holographic imaging of nonmetallic concentric pipes," *IEEE Trans. Instrum. Meas.*, vol. 69, no. 10, pp. 7594–7605, 2020.

[32] R. K. Amineh, M. Ravan, and R. Sharma, "Nondestructive testing of nonmetallic pipes using wideband microwave measurements," *IEEE Trans. Microwave Theory and Techniques*, vol. 65, no. 5, pp. 1763–1772, May 2020.

[33] M. Shah, Y. Gao, M. Ravan, and R. K. Amineh, "Quantitative defect size evaluation in fluid-carrying nonmetallic pipes," *IEEE Trans. Microwave Theory & Techniques,* vol. 70, no. 8, pp. 4071–4081, 2022.

[34] H. Wu and R. K. Amineh, "A low-cost and compact three-dimensional microwave holographic imaging system," *Electronics*, Special Issue on Applications of Electromagnetic Waves, vol. 8, no. 9, 2019.

[35] Y. Gao, M. Ravan, and R. K. Amineh, "Fast, robust, and low-cost microwave imaging of multiple non-metallic pipes," *Electronics*, vol. 10, no. 15, 2021.

[36] Y. Gao, M. Shah, and R. K. Amineh, "Assessment of eccentricity for multiple nonmetallic pipes using microwave sensing," *IEEE Trans. Instrum. Meas.*, vol. 71, no. 8000707, pp. 1–7, 2022.

Reza K. Amineh (Senior Member, IEEE, rkhalaja@nyit.edu) is currently an Associate Professor in the Department of Electrical and Computer Engineering at the New York Institute of Technology in New York, New York, USA. Prior to that, he was a Principal Scientist in the Department of Sensor Physics at Halliburton Co. He received his Ph.D. degree in electrical engineering from McMaster University in 2010. He was a post-doctoral fellow at the University of Toronto and McMaster University, from 2012 to 2013 and from 2010 to 2012, respectively. His research interests include applied electromagnetics with applications in imaging and sensing.